TÜBİTAK

Turkish Journal of Chemistry

http://journals.tubitak.gov.tr/chem/

Research Article

Turk J Chem
(2023) 47: 207-217
© TÜBİTAK
doi:10.55730/1300-0527.3530

Fabrication of dendritic PdCu alloy supported on 3D N-doped hollow graphene for efficient ethanol electrooxidation

Zhijie JIANG*, Shuiyuan FU*, Wei ZHAO, Xvtang LIU, Fei WANG, Mingyu CUI, Linyang DONG**
Jiangsu Province Engineering Research Center of Fine Utilization of Carbon Resources,
China University of Mining and Technology, Jiangsu, China

Received: 30.09.2022 • **Accepted/Published Online:** 29.11.2022 • **Final Version:** 20.02.2023

Abstract: Fabricating highly efficient Pd-based nanocatalysts with a well-defined structure is desired for the commercialization of direct ethanol fuel cell (DEFC). Herein, a series of hierarchical three-dimensional N-doped hollow graphene spheres (NHGS) supported dendritic PdCu alloy catalysts $Pd_xCu_{(d)}$-NHGS (x: Cu/Pd theoretical molar ratio of 4, 2, and 1) are assembled by one-pot ascorbic acid reduction-immobilization method. Aiming to maximize the Pd utilization and realize the efficient ethanol electrooxidation, this novel electrocatalyst offers potent activity sites and promotes electron and ion kinetics simultaneously. Characterization indicates that the as-obtained $Pd_4Cu_{(d)}$ alloy nanoparticles with average sizes of approximately 55 nm are evenly dispersed on the NHGS supporting materials obtained by using the SiO_2 nanospheres template strategy. Three catalysts all exhibit enhanced electrocatalytic activity, of which the $Pd_4Cu_{(d)}$-NHGS shows the highest mass current activity (2683 mA mg_{Pd}^{-1}), which is 2.59 times of the commercial Pd/C toward ethanol electrooxidation in alkaline medium. Based on the results, we believed that the $Pd_4Cu_{(d)}$-NHGS could exhibit extensive application prospect in alkaline DEFC.

Key words: Pd-based binary alloy, ethanol electrooxidation, N-doped hollow graphene, electrocatalysts

1. Introduction

Direct alcohol fuel cell (DAFC) is a low-temperature proton exchange membrane fuel cell (PEMFC) which could directly use low-carbon alcohols as fuel, such as methanol, ethanol, glycerol, and ethylene glycol [1-4]. Due to the easy storage and high energy conversion efficiency, DAFC has been considered as an ideal power source for portable electronic devices [5]. As a typical renewable fuel, ethanol has attracted extensive attention from researchers because of its high theoretical energy density (8 kWh/kg) [6], extensive biomass-derived availability, low toxicity, environmental friendliness, and low cost [7]. Therefore, direct ethanol fuel cell (DEFC) has developed exponentially in recent decades.

Until now, Pt and Pt-based catalysts have been regarded as the most potent electrocatalysts in electrooxidation of ethanol (EOR) [8, 9]. However, the rarity, prohibitive price, and CO poisoning of Pt all make it arduous to meet the commercial demands [10, 11]. Nowadays, Pd-based electrocatalysts, which are relatively cheaper, and more abundant, emerge as the appropriate alternative to Pt [12, 13], also exhibit excellent electrocatalytical performance and higher affinity for OH- than Pt-based catalysts in alkaline medium [14, 15]. Still, pure Pd catalysts inevitably suffer from low utilization efficiency and inadequate stability because of the poisoning intermediates formed in the reaction [16]. Previous studies have reported that the formation of bimetallic PdM or alloy by doping synergistic secondary metal elements can enhance the electrocatalytic activity and simultaneously reduce the use of precious metals, such as PdAu [17, 18] , PdAg [19, 20], PdNi [12, 21], PdSn [22], PdFe [23], PdCu [24-26], etc. The added metal could adsorb oxygen-containing active species at a lower potential to promote the further removal of the intermediate CO-like species from Pd surface. Besides, the synergistic effect that existed in the binary Pd-based alloys with proper atomic ratio could optimize the electronic structure and alter the d-band center of the alloy catalyst compared to the monometallic Pd counterparts, accordingly leading to the improvement of the antipoisoning ability and electrochemical properties [25, 27-29]. Because of the low cost and abundance, the benign metal of Cu, has attracted much attention. Pd nanoparticles possess high surface energy

* The authors contributed equally to this work.
** Correspondence: zhaow1965@163.com

and are very easy to agglomerate, which leads to lower catalyst utilization. Consequently, another alternative approach to fabricating high efficient catalysts is to disperse Pd-based nanoparticles on suitable supports [12, 13].

As a monolayer, hexatomic ring benzene-like structure carbon material, graphene possesses intriguing physical and chemical properties, including high theoretical specific surface area, superior electrical conductivities, excellent structural, and thermal stability. It was a promising carbon-based supporting material for anchoring Pd-based nanoelectrocatalysts in DEFC [30-32]. Two-dimensional (2D) graphene has displayed its unique advantages in current research. However, in practical applications the 2D graphene is unavoidably prone to stacking and self-agglomeration, which reduces the active surface area and hinders the electrolyte from spreading into the inside of the electrode [33, 34]. Therefore, it is feasible to design three-dimensional (3D) graphene with hollow structure through the SiO_2 hard template method to cope with the above obstacles [35, 36]. 3D graphene possesses larger specific surface area and also could provide more space for the transmission and storage of electrons, ions, and liquids in the electrolyte. Besides, due to its unique hollow structure and intrinsic properties of 2D graphene, it would further improve the conductivity of the graphene network and facilitate the even dispersion of alloy nanoparticles [37-39].

Lee et al. [40] prepared Pd networks supported on the 3D hollow graphene derived from SiO_2 nanospheres template method and applied it to formic acid electrooxidation. Liu et al. [33] reported the hollow N-doped graphene frameworks (HNGF) for supporting Pd NPs by using poly microspheres (glycidyl methacrylate) as templates. The resulting catalyst demonstrated high electrocatalytic activity and durability for methanol electrooxidation.

Particularly, the incorporation of the N atom into graphene structure, perhaps the most widely chosen method, can further tune the properties of the support since the N atom is of comparable atomic size and possesses available valence electrons to form valence bonds with carbon atoms [11]. Compared to the pristine graphene, doping N atom can improve graphene's conductivity and help anchor the binary alloy nanoparticles so as to enhance the catalytic activity [41, 42].

Motivated by these latest studies, we found that N-doped hollow structure graphene supported dendritic PdCu alloy catalyst for EOR in alkaline medium was barely reported. Herein, approximately 55 nm dendritic PdCu alloy nanoparticles with various molar ratios were synthesized and loaded on NHGS derived from the template method. Copper was used to lower noble metal Pd usage and to enhance EOR activity through a synergistic effect. The as-prepared PdCu alloy maintained a well-defined dendritic structure after loading on NHGS and other physical morphology, chemical composition, and valence states of the catalysts were analyzed in detail. Additionally, the electrocatalytic performance for EOR of the as-prepared catalysts were investigated by cyclic voltammetry (CV), chronoamperometric (CA), and linear scan voltammetry (LSV) measurements. Electrochemical evaluations demonstrated that $Pd_4Cu_{(d)}$-NHGS exhibited substantially excellent catalytic activity towards EOR, surpassing those of $Pd_2Cu_{(d)}$-NHGS, $Pd_1Cu_{(d)}$-NHGS, and Pd/C. This benefit from the optimized PdCu molar ratios and hollow microsphere structure in NHGS.

2. Experimental

2.1. Materials

Palladium chloride ($PdCl_2$) and tetraethyl orthosilicate (TEOS) was purchased from Macklin Co., Ltd. Copper chloride dihydrate ($CuCl_2.2H_2O$), sulfuric acid (98 wt% H_2SO_4), potassium permanganate ($KMnO_4$), hydrogen peroxide (30 wt% H_2O_2), sodium hydroxide (NaOH), ammonium solution, potassium bromide (KBr), ascorbic acid (AA), ethanol, and urea were purchased from Xi Long Chemical Co., Ltd (Guangzhou, China). Hexadecyltrimethyl ammonium bromide (CTAB, 99%) and 3-aminopropyl-trimethoxysilane (ATPS) were purchased from Aladdin Chemical Reagent Lo., Ltd. 10% Pd/C (Wako Pure Chemical Corporation) was used for comparison. Deionized (DI) water from Millipore was used throughout the experiment. All chemicals were used without any further purification.

2.2. Preparation of NHGS

Graphite oxide (GO) and SiO_2 nanospheres were prepared by the improved Hummers' method and modified Stöber method [43, 44]. After surface functionalization with ATPS, the functionalized SiO_2 and GO were added to 50 mL DI water at a mass ratio of 4:1. Then the solution was ultrasonicated for 2 h and constantly stirred for 12 h to let GO fully encapsulate the SiO_2 via electrostatic interaction. The solution was subsequently centrifuged to remove superfluous GO and then freeze-dried. The product was thermally calcined with urea in a tubular furnace at 700 °C for 2 h under N_2 atmosphere to obtain NG (nitrogen doped graphene)/SiO_2 composites. Finally, the composites were heated and refluxed in a 5 M NaOH solution to remove the SiO_2 template, the resulting product was washed several times with ethanol and DI water. NG was synthesized using the above thermally treated method.

2.3. Preparation of $PdCu_{(d)}$ alloy

First, $PdCl_2$ and NaCl were dissolved in DI water at a molar ratio of 1:2 and ultrasonicated for 2 h to obtain Na_2PdCl_4, then, 0.2 g CTAB, 0.18 g AA, and 0.10 g KBr were dissolved in 15 mL DI water in a 30 mL three-necked flask and stirred

for 15 min to blend evenly. The Na_2PdCl_4 and $CuCl_2$ were added successively with a Pd/Cu molar ratio of 1 (or 2, 4), and the suspension was heated rapidly to 90 °C under stirring for 1 h. After that, the dendritic $PdCu_{(d)}$ alloys were obtained by centrifugation and washed with DI water and ethanol.

2.4. Preparation of $PdCu_{(d)}$-NHGS

A series of $Pd_xCu_{(d)}$-NHGS were assembled by immobilizing $PdCu_{(d)}$ alloy on the as-prepared NHGS supports. First, 50 mg NHGS was dispersed in 80 mL DI water and sonicated for 20 min, followed by the addition of a certain amount of the above $PdCu_{(d)}$ alloy solution. The mixture was stirred for 4 h at room temperature. The resultant solution was centrifuged and washed three times with acetone and water and dried to obtain $Pd_4Cu_{(d)}$-NHGS, $Pd_2Cu_{(d)}$-NHGS, and $Pd_1Cu_{(d)}$-NHGS, respectively (Pd loadings of 4.1, 4.5, and 4.6 wt% by ICP). For comparison, $Pd_4C_{(d)}$-NG was obtained with the same procedure (Pd loadings of 4.8 wt% determined by ICP), and Pd-NG was prepared by $NaBH_4$ reduction method (Pd loadings of 5.2 wt% by ICP).

2.5. Structural characterization

The crystalline structure of catalysts and supports were analyzed by X-ray diffractometer (XRD, Bruker, D8-ADVANCE). The distribution of nanoparticles and microstructure of the as-prepared catalysts were examined by scanning electron microscopy equipped with an energy dispersive spectrometer (SEM-EDS, FEI, Quantan 250) and transmission electron microscope (TEM, FEI, Tecnai G2-F20), and the distribution of the elements were individually scanned. The particle sizes and morphology of template SiO_2 nanospheres were also observed by SEM. X-ray photoelectron spectroscopy (XPS) was carried out to investigate the surface composition and the chemical valence states of catalysts (Thermo Fisher, ESCALAB 250Xi). The PdCu molar ratio of the alloy samples were determined by laser ablation inductively coupled plasma mass (LA-ICP-MS, Agilent, NWR 213-7900).

2.6. Electrochemical measurements

The electrochemical measurements were conducted on CHI 660E workstation in a typical three-electrode cell at room temperature, including Ag/AgCl (saturated KCl) electrode and Pt foil (area: 1 cm×1 cm) electrode served as the reference electrode and counter electrode, and a glassy carbon electrode (GCE: φ = 3 mm) as the working electrode. Before the test, N_2 was blown through the electrolyte for 30 min to degas. The glassy carbon electrode was polished several times with 0.3 and 0.05 μm Al_2O_3 powder and washed with ethanol and DI water ultrasonically, and then dried for later use. As for the preparation of the working electrode, a mixture of 3 mg catalyst, 200 μL H_2O, 75 μL ethanol, and 25 μL Nafion (5 wt%) was ultrasonicated for 15 min to form an ink. Six microliters of the resulting ink was loaded on the GCE and dried at room temperature. The CV, i-t, and LSV tests were conducted in 1 M ethanol+1 M KOH solution at a sweep rate of 50 mV/s.

3. Results and discussion

3.1. Characterization of catalysts

As shown in Figure 1, The X-ray powder diffraction (XRD) patterns were measured to identify the as-prepared Pd-NG and $PdCu_{(d)}$-NHGS catalysts with different Pd/Cu ratios. The discernible diffraction peak around 26° is attributed to the (002) plane of graphitic carbon, which is the characteristic diffraction peak of graphene materials, consistent with the previous

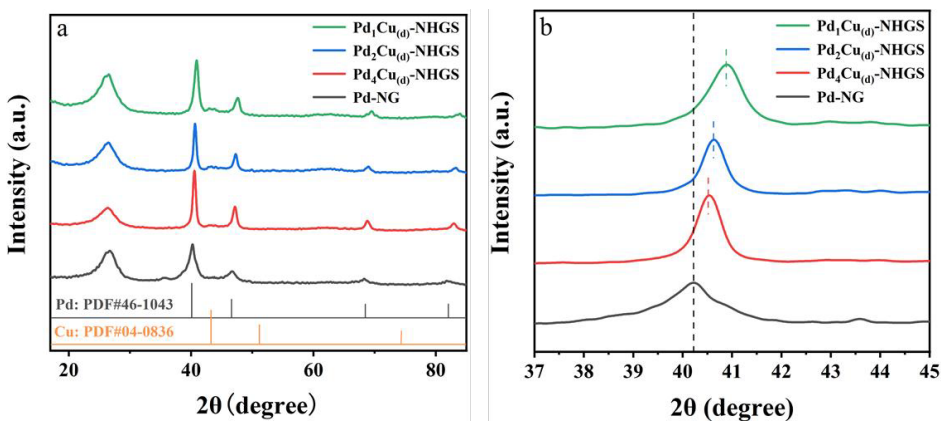

Figure 1. XRD patterns for the synthesized $Pd_4Cu_{(d)}$-NHGS, $Pd_2Cu_{(d)}$-NHGS, and $Pd_1Cu_{(d)}$-NHGS along with Pd-NG (a) and the enlarged patterns at around Pd (111) lattice plane (b).

studies [33, 45]. It is found that the peaks of face-centered cubic (fcc) Pd (111) appear prominently around 40.1°, 46.5°, and 68.2° (JCPDS No.46-1043), which are well matched by the diffraction peak of Pd/NG. For $PdCu_{(d)}$-NHGS catalysts (Figure 1a), compared with the standard card of Pd and Cu (JCPDS No.04-0836), all prominent intensive diffraction peaks of catalysts shifted and were located between the standard diffraction peaks of Pd and Cu (Figure 1b), which clearly indicated the alterations of the crystal structure and the generation of alloy [46].

Lattice parameters were obtained by using Bragg's law for the (111) and (220) planes.

$$2d \sin \theta = n \lambda \quad (1)$$

$$a = 2 \lambda / \sin \theta \quad (2)$$

where a is lattice parameter and λ is the wavelength of X-ray. Since the 2θ value of (111) plane may be influenced by the nearby peaks of NHGS, the lattice parameter of alloy has been calculated for all the binary catalysts from the θ values of (220) plane.

Both Pd and Cu possess an fcc crystal structure. According to Vegard's law, the lattice parameters of the PdCu alloys decreased with the increase of the incorporation of Cu [11, 47]. The lattice parameters of the binary PdCu alloy were calculated based on the XRD data. The mathematical expression can be given as

$$a_{al} = a_A (1-x) + a_B x \quad (3)$$

Here, a_{al}, a_A, a_B and x are the lattice parameters of alloy, host metal A, cometal B, and fractional content of B in the A, respectively. By applying the obtained "a" of PdCu alloy, the degree of alloying (Da) could be calculated.

$$Da = (a - a_0)/(a_{al} - a_0) \quad (4)$$

where a, a_{al} and a_0 represent the lattice parameter of the particular alloy catalyst, the theoretically calculated lattice parameter assuming that all the Cu is alloyed, and the lattice parameter Pd NPs, respectively. The calculated d-spacing for the strongest peak (111) of Pd-NG is 2.246 Å, which is consistent with the value in the report (JCPDS-05-0681). The molar ratios of Pd to Cu determined by ICP, the d-spacing, and the lattice parameter of the PdCu alloyed catalysts were summarized and presented in Table S1. The calculated Da of $Pd_4Cu_{(d)}$-NHGS, $Pd_2Cu_{(d)}$-NHGS, and $Pd_1Cu_{(d)}$-NHGS are 54.17%, 59.75% and 71.91%, respectively. With increasing Cu concentrations in Pd lattice, the d-spacing of alloy decreased since Pd possesses a bigger atomic diameter than Cu. The optimal alloying degree indicated the formation of homogeneous solid solution within the Pd and Cu, which can facilitate the modifications of the d band center and electronic properties of alloy [48].

Raman spectroscopy is used to further study the structure of graphene support and catalysts. As shown in Figure 2, the as-prepared GO, NG, NHGS, $PdCu_{(d)}$-NG, and $PdCu_{(d)}$-NHGS all exhibit two characteristic peaks corresponding to the D band and G band of graphene materials around 1344 cm^{-1} and 1590 cm^{-1}. The G peak is related to the degree of graphitization, which arises from the in-plane stretching motion of pristine sp^2 carbon atom pairs. While the D band is associated with the defects which disrupt sp^2 carbon rings caused by the incorporation of oxygen-containing bonds [11, 25].

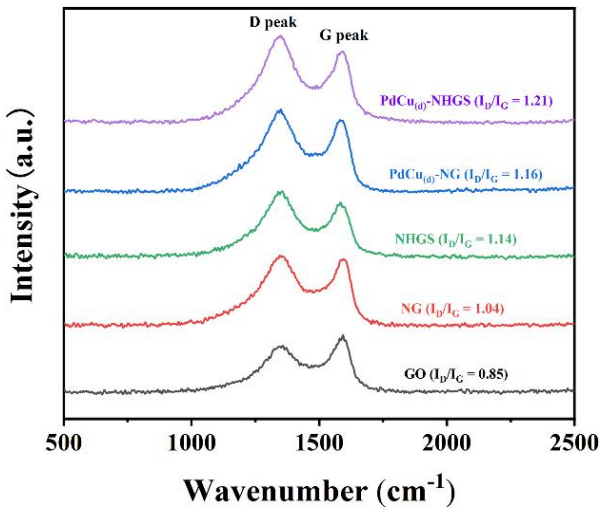

Figure 2. Raman spectra of GO, NG, NHGS, $PdCu_{(d)}$-NG, and $PdCu_{(d)}$-NHGS.

Additionally, the intensity ratio of D and G peaks (I_D/I_G) can relatively measure the degree of defects in graphite structure. The I_D/I_G values of all the catalysts follow the order: GO (0.85) < NG (1.04) < NHGS (1.14) < $PdCu_{(d)}$-NG (1.16) < $PdCu_{(d)}$-NHGS (1.21). The high I_D/I_G value means an increased defect sites, which will offer more anchoring sites on the support to improve the dispersity and stability of the PdCu alloy, leading to better electrocatalytic performance [11].

SEM-EDS and TEM were carried out to investigate the morphology and element distribution of the catalysts, supports, and template. Figures 3a and 3b show the SEM images of SiO_2 and NHGS. The synthesized SiO_2 nanospheres have a uniform size distribution with an average size of 220–240 nm, this also could be observed in the TEM image of SiO_2 (Figure S1a). The NHGS support was obtained after the removal of the SiO_2 template and had a hollow structure. TEM images of $Pd_4Cu_{(d)}$-NG and $Pd_4Cu_{(d)}$-NHGS are depicted in Figures 3c and 3d. The NG nanosheets obviously wrinkled and aggregated, which would affect the dispersity of the PdCu alloy. The TEM image of $Pd_4Cu_{(d)}$-NHGS clearly shows the hollow structure of NHGS. The hollow structure can effectively inhibit the aggregation of graphene nanosheets so as to promote the anchorage and dispersion of alloy nanoparticles.

Furthermore, the SEM-EDS elemental mapping image (Figures 3e and 3f) reveals the even distribution of carbon, oxygen, palladium, and copper. The EDS results indicate that the molar ratio of Pd and Cu in $Pd_4Cu_{(d)}$-NHGS is approximately 3:1, which roughly agrees with the ICP result. Figure 3h exhibits the well-defined dendritic morphology of the as-prepared PdCu alloy, with the size around 55 nm. And this hierarchical dendritic structure is relevant to the influence of the structure-directing agent, CTAB, which is consistent with the previous studies [46]. Moreover, the PdCu alloy nanoparticles are better dispersed on the NHGS than unsupported PdCu alloy sample (Figures 3g and S1b), suggesting that the highly interconnected hollow structure of graphene is more beneficial for the uniform distribution of the binary alloy nanoparticle and is critical for the facile electron transport simultaneously.

To further investigate the structure, XPS characterization was conducted to precisely explore the surface composition and the chemical valence states of the $PdCu_{(d)}$-NHGS catalysts. As shown in Figure 4, it can confirm the existence of C, O, N, Pd, and Cu elements in the $PdCu_{(d)}$-NHGS and Pd-NG composites. The C1s spectra of the supports NHGS consist of three peaks corresponding to C-C, C-N, and C=O (Figure 4a), which are located at binding energy around 284.7 eV, 285.8 eV, and 286.7 eV, respectively [12]. The content of the C=O bond only accounted for a small portion in NHGS, signifying that the oxygen-containing functional groups in GO were mostly reduced during the thermal calcination. The presence of the C–N bond suggests that N atoms were successfully incorporated into graphene structure. The N 1s peak could be deconvoluted into three characteristic peaks at binding energy around 398.4 eV, 399.9 eV, and 401.8eV, corresponding to pyridinic N, pyrrolic N, and graphitic N, respectively [41]. The specific contributions of the above three N species to the total doped nitrogen were calculated based on the fitted N 1s curve (Figure 4b), which were 53.52%, 35.66%, and 10.82%, respectively.

Pd 3d spectra mainly contains two broad peaks emerged at binding energy around 336 and 341 eV in Pd-NG and $Pd_4Cu_{(d)}$-NHGS as presented in Figure S2. The spectra could be deconvoluted to two groups of peaks at binding energy 335.3 and 336.7, 340.6 and342.2 eV, assigned to the Pd $3d_{5/2}$ and Pd $3d_{3/2}$ states of Pd^0 and Pd^{2+} species on the surface of

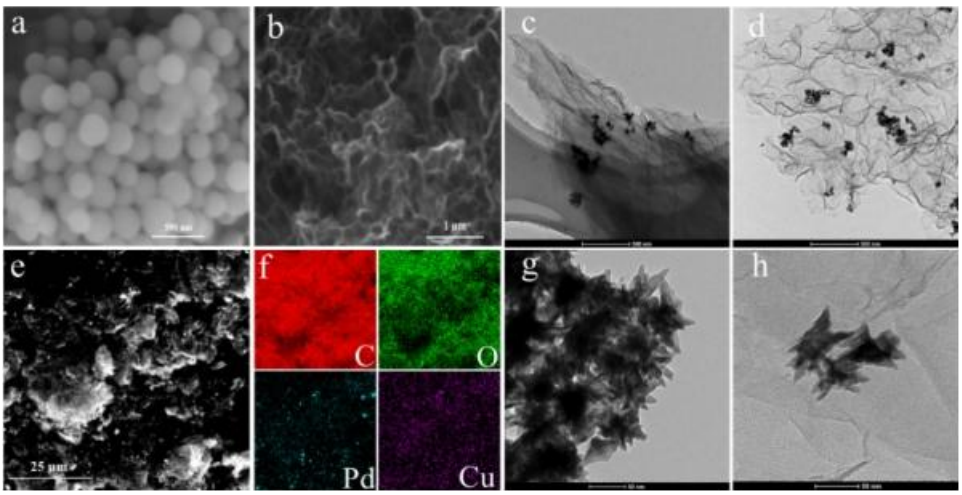

Figure 3. SEM of SiO_2 and NHGS (a, b), TEM of $Pd_4Cu_{(d)}$-NG (c), $Pd_4Cu_{(d)}$-NHGS (d), SEM of $Pd_4Cu_{(d)}$-NHGS and the elemental mappings of C, O, Pd, Cu (e, f) and PdCu alloy (g, h).

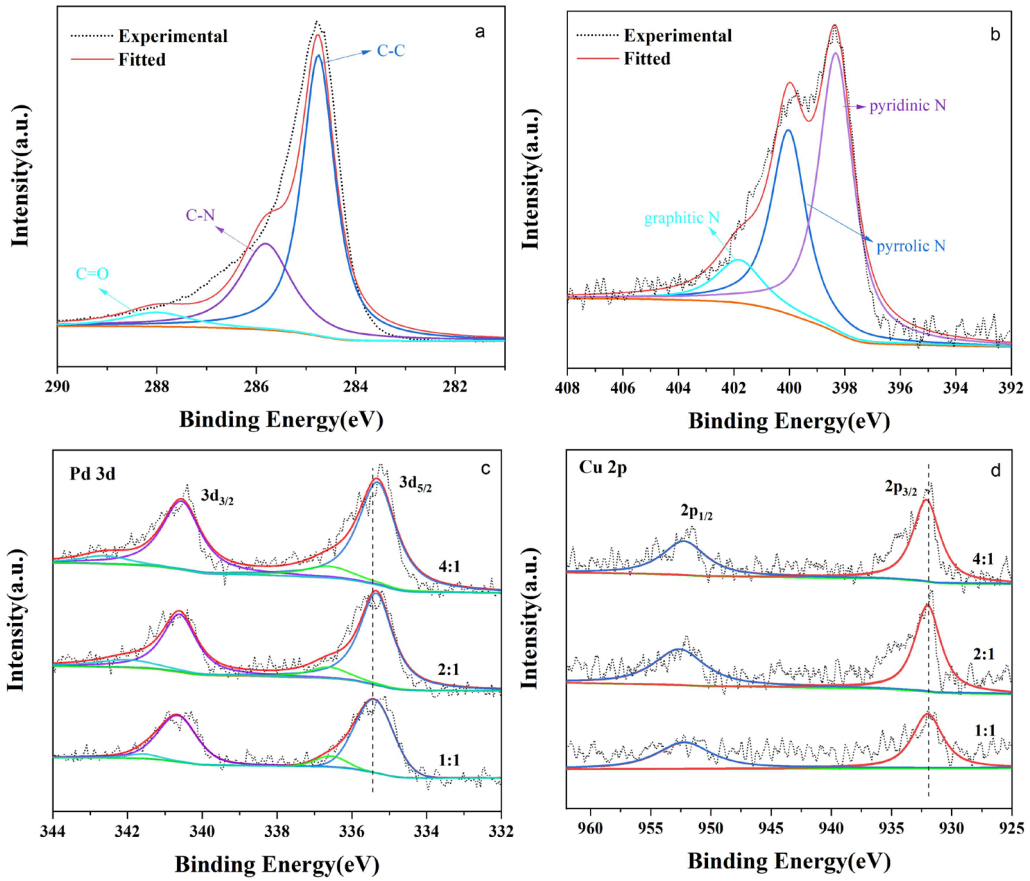

Figure 4. XPS spectra of the C 1s and N 1s (a, b), XPS spectra of Pd 3d and Cu 2p for the PdCu-NHGS (c, d).

$PdCu_{(d)}$-NHGS [49]. As shown in Figures 4c and 4d, the deconvolution of Pd and Cu in $PdCu_{(d)}$-NHGS with different Pd/Cu molar ratios were measured, the Pd^0 and Cu^0 species are predominant (approximately 70%) compared to the Pd^{2+} and Cu^{2+} in all prepared catalyst. The slight negative shift of the Pd $3d_{5/2}$ binding energy relative to the Pd-NG is observed, implying the increased electron density. Additionally, the positive shift was observed in Cu $2p_{3/2}$ binding energy compared to the standard Cu 2p XPS data, which confirms the electron transfer from Cu to Pd [27, 50]. This kind of electron transfer can decrease the d-band energy of Pd, hence facilitating the desorption of the poisonous intermediates and regeneration of the active sites during the electrooxidation of ethanol [51].

3.2. Electrochemical analysis

The electrocatalytic performance of the as-prepared catalysts toward EOR in alkaline medium was evaluated by CV tests carried out in 1.0 M NaOH solution with and without 1.0 M C_2H_5OH at a scan rate of 50 mV/s. To obtain the electrochemical surface area (ECSA) of the catalysts, the CV curves normalized by the Pd mass were measured in a 1.0 M NaOH solution saturated with N_2, as shown in Figure 5. The ECSA of catalysts were calculated by the integral area of the reduction of palladium oxide monolayer around –0.25V based on the following equation:

$$ECSA = Q_0/405 \times m,$$

where m (mg), Q (mC), and 405 (C/cm^2) represent the mass of Pd on GCE, the total reduction charge of the PdO, and the monolayer PdO reduction charge constant, respectively. The ECSA of $Pd_4Cu_{(d)}$-NHGS was approximately estimated to be 59.2 $m^2 g^{-1}$, which was larger than those of $Pd_2Cu_{(d)}$-NHGS (41.5 $m^2 g^{-1}$) and $Pd_1Cu_{(d)}$-NHGS (37.9 $m^2 g^{-1}$), and 2.4 times higher than commercial 10 % Pd/C (24.2 $m^2 g^{-1}_{Pd}$). The higher ECSA of $Pd_4Cu_{(d)}$-NHGS could be attributed to the uniform distribution of the alloy nanoparticles on NHGS. Moreover, the branched structure of the alloy can also expose more effective active sites, which is also the advantage of the dendritic alloy catalyst.

The CV curves of the prepared catalyst were measured in N_2-saturated 1.0 M NaOH + 1M C_2H_5OH solution and normalized by the mass activity of Pd, exhibited in Figure 6. Two typical sharp peaks are observed in the forward and backward scans of all catalysts. The characteristic oxidation peak in the forward scan was generated owing to the oxidation

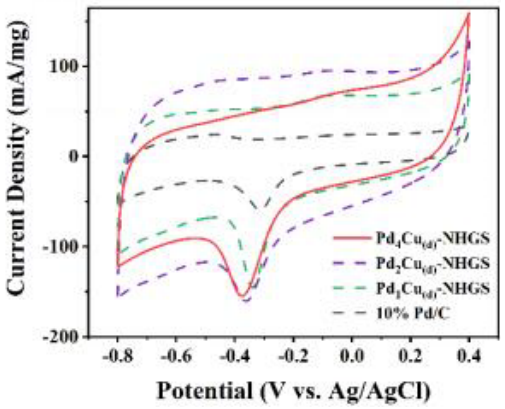

Figure 5. CV curves of different $PdCu_{(d)}$-NHGS and commercial Pd/C in 1 M NaOH solution.

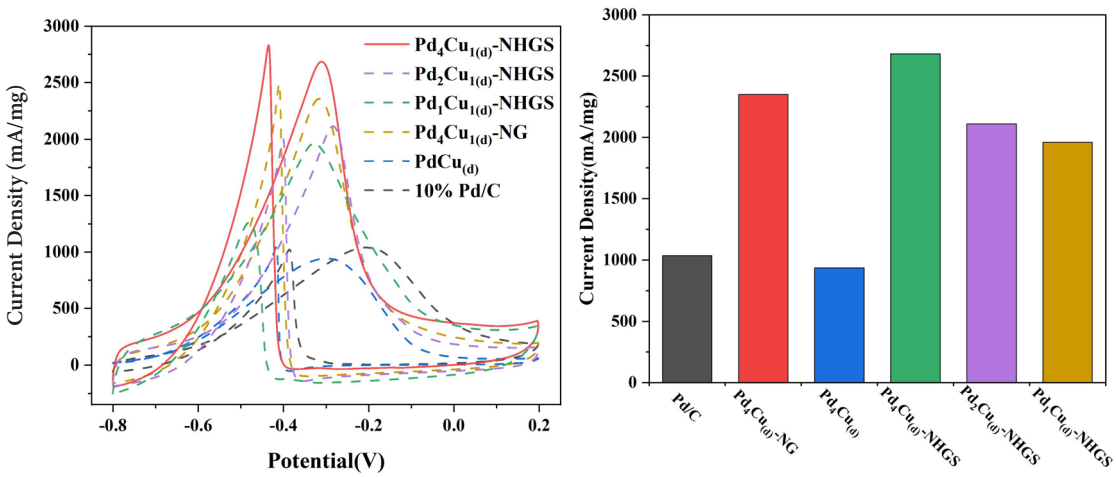

Figure 6. CV curves (a) and the forward peak current density (b) of three $PdCu_{(d)}$-NHGS, $PdCu_{(d)}$-NG, $PdCu_{(d)}$ and commercial Pd/C in 1 M CH_3CH_2OH + 1 M NaOH.

of the absorbed ethanol. The peak in the backward scan was ascribed to the oxidation of carbonaceous intermediates, which were incompletely oxidized in the forward scan [12, 52]. The current density in the forward scan of $Pd_4Cu_{(d)}$-NHGS reaches 2683 mA/mg, which is higher than those of $Pd_2Cu_{(d)}$-NHGS (2110 mA/mg), $Pd_1Cu_{(d)}$-NHGS (1958 mA/mg) and $Pd_4Cu_{1(d)}$-NG (2343 mA/mg) and is 2.86 and 2.59 times of $Pd_4Cu_{(d)}$ (937 mA/mg) and Pd/C (1036 mA/mg), indicating that the electrocatalytic activity for EOR could be regulated by changing the PdCu alloy composition. And $Pd_4Cu_{(d)}$-NHGS possesses significantly higher current density at the same Pd loadings than pure PdCu alloy and commercial Pd/C. Also, the current density of $Pd_4Cu_{(d)}$-NHGS is comparable to or even greater than the recently reported Pd based catalysts, as shown in Table S2.

The presence of Cu in the alloy would facilitate the absorption of oxygenated species, e.g., OH_{ads} at lower potential and thus favors the oxidation of the intermediate product adsorbed on the active sites of the catalyst [32]. Therefore, the synergistic effect of Pd and Cu in $PdCu_{(d)}$-NHGS and the presence of oxygen-containing functional groups in NHGS efficiently reduce the poisoning of intermediate products and release more active sites to promote the reaction. However, high Cu content would lead to excessive OH_{ads} coverage on the surface, hindering the adsorption of ethanol and seemingly rendering the decrease of the catalyst activity [16], which is consistent with the CV results.

The onset potential (E_o) and Tafel slope, which are two essential parameters to evaluate the EOR kinetics, were measured by linear scan voltammetry (LSV) tests. As shown in Figure 7a, compared to commercial 10% Pd/C, all dendritic PdCu-based catalysts show distinct negative-shifted onset potentials, among which the $PdCu_{(d)}$-NHGS exhibited the lowest onset potential, signifying that ethanol was more easily oxidized and the reaction kinetics of alloy was enhanced [53].

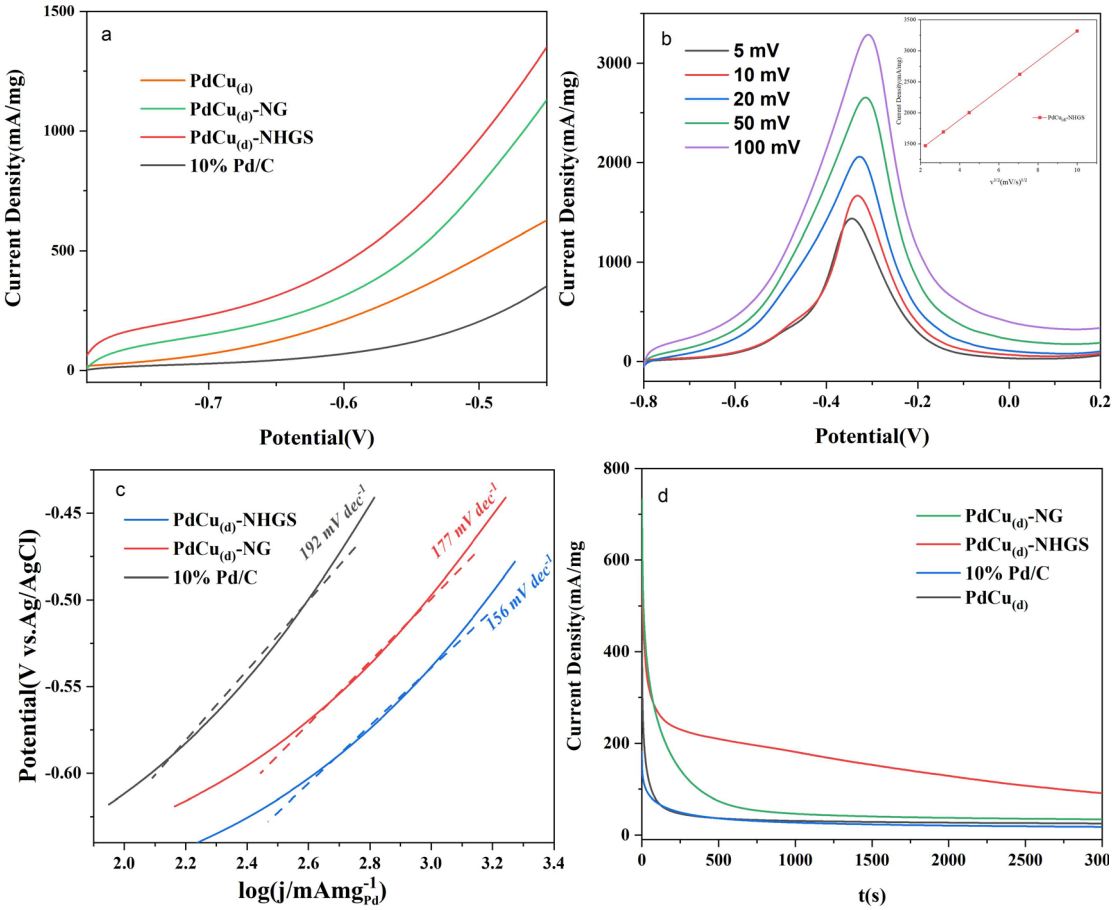

Figure 7. LSV curves of $PdCu_{(d)}$-NHGS, $PdCu_{(d)}$-NG, $PdCu_{(d)}$ and commercial Pd/C in 1 M CH_3CH_2OH + 1 M NaOH (a), LSV curves of the $Pd_4Cu_{(d)}$-NHGS at different scan rates and the inset curve is the linear relationship between peak current density and the square root of the scanning rate (b), Tafel plots of $PdCu_{(d)}$-NHGS, $PdCu_{(d)}$-NG, and commercial Pd/C in 1 M CH_3CH_2OH + 1 M NaOH (c), i-t curves of $PdCu_{(d)}$-NHGS, $PdCu_{(d)}$-NG, $PdCu_{(d)}$, and commercial Pd/C in 1 M CH_3CH_2OH + 1 M NaOH at –0.45V vs. Ag/AgCl (d).

As shown in Figure 7b and its inert figure are the LSV curves of the $PdCu_{(d)}$-NHGS at different scan rates and the linear relationship between the square root of scanning rates and the corresponding peak current density. The peak current density of the ethanol oxidation peak increased with the increase of the scan rate, and the corresponding peak potential also shifted positively, indicating that the process is reversible and the kinetics of catalytic EOR in alkaline medium is controlled by the diffusion process [54].

Besides, the kinetics of EOR was further investigated by the Tafel slope, as shown in Figure 7c. The fitted Tafel slopes diminished in the order: commercial Pd/C > $PdCu_{(d)}$-NG > $PdCu_{(d)}$-NHGS. The lower value of Tafel slopes implies the faster transfer of active substances and electrons on the catalyst. Accordingly, the kinetics of OH^- adsorbed on the $PdCu_{(d)}$-NHGS is the fastest in the alkaline medium. The hollow structure of NHGS is conducive to the mass transfer process and accelerates the oxidation.

To evaluate the electrochemical stability of these four catalysts toward EOR, the chronoamperometry (CA) tests were measured at –0.45 V vs. Ag/AgCl in a N_2 saturated 1 M ethanol + 1 M NaOH solution for 3000s. As shown in Figure 7d, the obtained i-t curves reveal that all the polarization currents decay rapidly at the preliminary stage and then deceased gradually [55], and the rates of decay for $PdCu_{(d)}$-NHGS and $PdCu_{(d)}$-NHGS were obviously smaller than the pure PdCu alloy and the commercial Pd/C. At the end of 3000 s, the $PdCu_{(d)}$-NHGS still possessed the highest current density among all these catalysts under the same conditions due to better dispersion on the NHGS supports. Meanwhile, the highest long-term electrocatalytic stability of $PdCu_{(d)}$-NHGS also suggested that the combination of NHGS and alloy enhanced the tolerance against poisonous intermediates for EOR in alkaline media.

4. Conclusion

In summary, a series of dendritic PdCu alloy nanoparticles has been synthesized with the help of CTAB as structure-directing agent and ascorbic acid as a reducing agent, and the morphology and dispersion of the catalysts were determined by XRD, XPS, SEM, and TEM. To reduce the consumption of precious metal Pd and simultaneously achieve the synergy of PdCu, the optimum composition of alloy was explored, and the novel graphene material NHGS was introduced as the superior support. According to the electrochemical results, the $Pd_4Cu_{(d)}$-NHGS exhibited the highest current density among all the as-prepared catalysts. Additionally, it also demonstrated the better kinetics and stability than the Pd-NG and commercial Pd/C toward EOR in alkaline media, which was correlated with the presence of Cu and the N-doped hollow graphene structure. We believe that this work could offer new insights into fabricate high performance Pd-based electrocatalysts for EOR, which will contribute to the development of DEFCs applications.

Conflict of interest

The authors declare that they have no known competing financial interests or personal relationships that could have appeared to influence the work reported in this paper.

Acknowledgments

This work was supported by the key research and development program of Xuzhou (KC21127) and Priority Academic Program Development of Jiangsu Higher Education Institutions.

References

1. Bianchini C, Shen PK. Palladium-based electrocatalysts for alcohol oxidation in half cells and in direct alcohol fuel cells. Chemical Reviews 2009; 109: 4183-4206. https://doi.org/10.1021/cr9000995

2. Arico AS, Srinivasan S, Antonucci V. DMFCs: from fundamental aspects to technology development. Fuel Cells 2001; 1: 133-161. https://doi.org/10.1002/1615-6854(200107)1:2<133::AID-FUCE133>3.0.CO;2-5

3. Holade Y, Morais C, Arrii-Clacens S, Servat K, Napporn TW et al. New preparation of PdNi/C and PdAg/C nanocatalysts for glycerol electrooxidation in alkaline medium. Electrocatalysis 2013; 4: 167-178. https://doi.org/10.1007/s12678-013-0138-1

4. Rousseau S, Coutanceau C, Lamy C, Leger JM. Direct ethanol fuel cell (DEFC): Electrical performances and reaction products distribution under operating conditions with different platinum-based anodes. Journal of Power Sources 2006; 158: 18-24. https://doi.org/10.1016/j.jpowsour.2005.08.027

5. Xu H, Song PP, Fernandez C, Wang J, Zhu MS et al. Sophisticated construction of binary pdpb alloy nanocubes as robust electrocatalysts toward ethylene glycol and glycerol oxidation. ACS Applied Materials & Interfaces 2018; 10: 12659-12665. https://doi.org/10.1021/acsami.8b00532

6. Erini N, Loukrakpam R, Petkov V, Baranova EA, Yang RZ et al. Ethanol electro-oxidation on ternary platinum-rhodium-tin nanocatalysts: insights in the atomic 3D structure of the active catalytic phase. ACS Catalysis 2014; 4: 1859-1867. https://doi.org/10.1021/cs500147p

7. Dutta A, Datta J. Outstanding catalyst performance of PdAuNi nanoparticles for the anodic reaction in an alkaline direct ethanol (with anion-exchange membrane) fuel cell. Journal of Physical Chemistry C 2012; 116: 25677-25688. https://doi.org/10.1021/jp305323s

8. Porter NS, Wu H, Quan ZW, Fang JY. Shape-control and electrocatalytic activity-enhancement of pt-based bimetallic nanocrystals. Accounts of Chemical Research 2013; 46: 1867-1877. https://doi.org/10.1021/ar3002238

9. Bhunia K, Khilari S, Pradhan D. Monodispersed PtPdNi trimetallic nanoparticles-integrated reduced graphene oxide hybrid platform for direct alcohol fuel cell. ACS Sustainable Chemistry & Engineering 2018; 6: 7769-7778. https://doi.org/10.1021/acssuschemeng.8b00721

10. Song PP, Xu H, Wang J, Zhang YP, Gao F et al. 1D alloy ultrafine Pt-Fe nanowires as efficient electrocatalysts for alcohol electrooxidation in alkaline media. Nanoscale 2018; 10: 16468-16473. https://doi.org/10.1039/c8nr04918a

11. Chowdhury SR, Maiyalagan T, Bhattachraya SK, Gayen A. Influence of phosphorus on the electrocatalytic activity of palladium nickel nanoalloy supported on N-doped reduced graphene oxide for ethanol oxidation reaction. Electrochimica Acta 2020; 342. https://doi.org/10.1016/j.electacta.2020.136028

12. Zhang MM, Li Y, Pan DH, Yan ZX, Meng SC et al. Nickel core-palladium shell nanoparticles grown on nitrogen-doped graphene with enhanced electrocatalytic performance for ethanol oxidation. RSC Advances 2016; 6: 33231-33239. https://doi.org/10.1039/c6ra06416g

13. Tan JL, De Jesus AM, Chua SL, Sanetuntikul J, Shanmugam S et al. Preparation and characterization of palladium-nickel on graphene oxide support as anode catalyst for alkaline direct ethanol fuel cell. Applied Catalysis A-General 2017; 531: 29-35. https://doi.org/10.1016/j.apcata.2016.11.034

14. Carrera-Cerritos R, Fuentes-Ramirez R, Cuevas-Muniz FM, Ledesma-Garcia J, Arriaga LG. Performance and stability of Pd nanostructures in an alkaline direct ethanol fuel cell. Journal of Power Sources 2014; 269: 370-378. https://doi.org/10.1016/j.jpowsour.2014.06.161

15. Zheng Y, Wan XJ, Cheng X, Cheng K, Dai ZF et al. Advanced catalytic materials for ethanol oxidation in direct ethanol fuel cells. Catalysts 2020; 10. https://doi.org/10.3390/catal10020166

16. Serov A, Asset T, Padilla M, Matanovic I, Martinez U et al. Highly-active Pd-Cu electrocatalysts for oxidation of ubiquitous oxygenated fuels. Applied Catalysis B-Environmental 2016; 191: 76-85. https://doi.org/10.1016/j.apcatb.2016.03.016

17. Chen LY, Chen N, Hou Y, Wang ZC, Lv SH et al. Geometrically Controlled Nanoporous PdAu Bimetallic Catalysts with Tunable Pd/Au Ratio for Direct Ethanol Fuel Cells. ACS Catalysis 2013; 3: 1220-1230. https://doi.org/10.1021/cs400135k

18. Kottayintavida R, Gopalan NK. PdAu alloy nano wires for the elevated alcohol electro-oxidation reaction. Electrochimica Acta 2021; 384. https://doi.org/10.1016/j.electacta.2021.138405

19. Adam A, Adam MI, Zhang CM, Haruna B, Chi MZ et al. Ternary supportless Pd@Cd-Ag core-shell as advanced nanocatalysts towards electro-oxidation performance of ethanol. Journal Of Alloys And Compounds 2021; 868. https://doi.org/10.1016/j.jallcom.2021.158955

20. Cui ZQ, Hu JW, Jiang XM, Zhang DL, Fang CH. Asymmetric Au/(PdAg alloy) nano-allium giganteums for their enhanced electrocatalytic performances to ethanol oxidation reaction. Journal of Alloys And Compounds 2021; 855. https://doi.org/10.1016/j.jallcom.2020.157385

21. Wang Y, Shi FF, Yang YY, Cai WB. Carbon supported Pd-Ni-P nanoalloy as an efficient catalyst for ethanol electro-oxidation in alkaline media. Journal of Power Sources 2013; 243: 369-373. https://doi.org/10.1016/j.jpowsour.2013.06.021

22. Cao ZS, Liu XH, Meng XZ, Cai L, Chen JY et al. Synthesis of bimetallic PdSn nanoparticle assembly as highly efficient electrocatalyst for ethanol oxidation. Colloids and Surfaces A-Physicochemical and Engineering Aspects 2021; 621. https://doi.org/10.1016/j.colsurfa.2021.126577

23. Wang YR, He QL, Guo J, Wang JM, Luo ZP et al. Ultrafine FePd nanoalloys decorated multiwalled cabon nanotubes toward enhanced ethanol oxidation reaction. ACS Applied Materials & Interfaces 2015; 7: 23920-23931. https://doi.org/10.1021/acsami.5b06194

24. Cheng YZ, Xue J, Yang M, Li HL, Guo PZ. Bimetallic PdCu nanoparticles for electrocatalysis: multiphase or homogeneous alloy? Inorganic Chemistry 2020; 59: 10611-10619. https://doi.org/10.1021/acs.inorgchem.0c01056

25. Ye N, Jiang Z, Fang T. Assembling the PdCu/rGO catalysts for methanol oxidation reaction in alkaline media by tuning the electronic structure. Electrochimica Acta 2020; 352. https://doi.org/10.1016/j.electacta.2020.136473

26. Fan JC, Yu SS, Qi K, Liu C, Zhang L et al. Synthesis of ultrathin wrinkle-free PdCu alloy nanosheets for modulating d-band electrons for efficient methanol oxidation. Journal of Materials Chemistry A 2018, 6: 8531-8536. https://doi.org/10.1039/c8ta01912f

27. Wang HJ, Zhang SL, Cai WW, Xu BZ, Cai ZX et al. Largely boosted methanol electrooxidation using ionic liquid/PdCu aerogels via interface engineering. Materials Horizons 2020; 7: 2407-2413. https://doi.org/10.1039/d0mh00646g

28. Luo SS, Wang R, Hei P, Gao LL, Yang JY et al. Self-assembled Ni_2P nanosheet-implanted reduced graphene oxide composite as highly efficient electrocatalyst for oxygen evolution reaction. Colloids and Surfaces A-Physicochemical and Engineering Aspects 2021; 612. https://doi.org/10.1016/j.colsurfa.2020.125992

29. Lao XZ, Yang M, Chen JY, Zhang LY, Guo PZ. The ethanol oxidation reaction on bimetallic Pd_xAg_1-x nanosheets in alkaline media and their mechanism study. Electrochimica Acta 2021; 374. https://doi.org/10.1016/j.electacta.2021.137912

30. Pei SF, Wei QW, Huang K, Cheng HM, Ren WC. Green synthesis of graphene oxide by seconds timescale water electrolytic oxidation. Nature Communications 2018; 9. https://doi.org/10.1038/s41467-017-02479-z

31. Jiang YY, Lu YZ, Li FH, Wu TS, Niu L et al. Facile electrochemical codeposition of "clean" graphene-Pd nanocomposite as an anode catalyst for formic acid electrooxidation. Electrochemistry Communications 2012; 19: 21-24. https://doi.org/10.1016/j.elecom.2012.02.035

32. Hu J, Wu XF, Zhang QF, Gao MY, Qiu HF et al. Highly active PdNi/RGO/Polyoxometalate Nanocomposite Electrocatalyst for Alcohol Oxidation. Langmuir 2018; 34: 2685-2691. https://doi.org/10.1021/acs.langmuir.7b04031

33. Liu Q, Lin Y, Fan JC, Lv D, Min YL et al. Well-dispersed palladium nanoparticles on three-dimensional hollow N-doped graphene frameworks for enhancement of methanol electro-oxidation. Electrochemistry Communications 2016; 73: 75-79. https://doi.org/10.1016/j.elecom.2016.10.017

34. Jiang LL, Fan ZJ. Design of advanced porous graphene materials: from graphene nanomesh to 3D architectures. Nanoscale 2014; 6: 1922-1945. https://doi.org/10.1039/c3nr04555b

35. Thangavel R, Kannan AG, Ponraj R, Yoon G, Aravindan V et al. Surface enriched graphene hollow spheres towards building ultra-high power sodium-ion capacitor with long durability. Energy Storage Materials 2020; 27: 599-599. https://doi.org/10.1016/j.ensm.2019.09.016

36. Huang XD, Qian K, Yang J, Zhang J, Li L et al. Functional Nanoporous Graphene Foams with Controlled Pore Sizes. Advanced Materials 2012; 24: 4419-4423. https://doi.org/10.1002/adma.201201680

37. Yan ZQ, Yao WL, Hu L, Liu DD, Wang CD et al. Progress in the preparation and application of three-dimensional graphene-based porous nanocomposites. Nanoscale 2015; 7: 5563-5577. https://doi.org/10.1039/c5nr00030k

38. Zhang RJ, Hu RR, Li XM, Zhen Z, Xu ZH et al. A Bubble-derived strategy to prepare multiple graphene-based porous materials. Advanced Functional Materials 2018; 28. https://doi.org/10.1002/adfm.201705879

39. Maiyalagan T, Dong XC, Chen P, Wang X. Electrodeposited Pt on three-dimensional interconnected graphene as a free-standing electrode for fuel cell application. Journal of Materials Chemistry 2012; 22: 5286-5290. https://doi.org/10.1039/c2jm16541d

40. Qiu XY, Wu P, Xu L, Tang YW, Lee JM. 3D Graphene hollow nanospheres @ palladium-networks as an efficient electrocatalyst for formic acid oxidation. Advanced Materials Interfaces 2015; 2. https://doi.org/10.1002/admi.201500321

41. Chowdhury SR, Maiyalagan T. Enhanced electro-catalytic activity of nitrogen-doped reduced graphene oxide supported PdCu nanoparticles for formic acid electro-oxidation. International Journal of Hydrogen Energy 2019, 44: 14808-14819. https://doi.org/10.1016/j.ijhydene.2019.04.025

42. Chai GL, Qiu KP, Qiao M, Titirici MM, Shang CX et al. Active sites engineering leads to exceptional ORR and OER bifunctionality in P,N Co-doped graphene frameworks. Energy & Environmental Science 2017; 10: 1186-1195. https://doi.org/10.1039/c6ee03446b

43. Marcano D.C, Kosynkin DV, Berlin JM, Sinitskii A, Sun ZZ et al. Improved Synthesis of Graphene Oxide (vol 4, pg 4806, 2010). ACS NANO 2018; 12: 2078-2078. https://doi.org/10.1021/acsnano.8b00128

44. Fang XL, Chen C, Liu ZH, Liu PX, Zheng NF. A cationic surfactant assisted selective etching strategy to hollow mesoporous silica spheres. Nanoscale 2011; 3: 1632-1639. https://doi.org/10.1039/c0nr00893a

45. Zhang JY, Feng AN, Bai J, Tan ZB, Shao WY et al. One-pot synthesis of hierarchical flower-like Pd-Cu alloy support on graphene towards ethanol oxidation. Nanoscale Research Letters 2017; 12. https://doi.org/10.1186/s11671-017-2290-7

46. Zuo YP, Rao DW, Li S, Li TT, Zhu GL et al. Atomic vacancies control of Pd-based catalysts for enhanced electrochemical performance. Advanced Materials 2018; 30. https://doi.org/10.1002/adma.201704171

47. Chen RN, Sun MX, Pang GG, Zhou JS, Hou L et al. Highly active PdCu alloy nanowire network electrocatalyst for ethanol and methanol electrooxidation. Chemelectrochem 2017; 4: 1081-1087. https://doi.org/10.1002/celc.201700058

48. Varshney M, Sharma A, Shin H, Lee HH, Jeon T et al. Influence of Ni doping on PtNi nanoparticles: Synthesis, electronic/atomic structure and photocatalyst investigations. Journal of Physics and Chemistry of Solids 2017; 110: 187-194. https://doi.org/10.1016/j.jpcs.2017.06.012

49. Yang NL, Zhang ZC, Chen B, Huang Y, Chen JZ et al. Synthesis of ultrathin pdcu alloy nanosheets used as a highly efficient electrocatalyst for formic acid Oxidation. Advanced Materials 2017; 29. https://doi.org/10.1002/adma.201700769

50. Li J, Song Y, Wang YN, Zhang H. Ultrafine PdCu nanoclusters by ultrasonic-assisted reduction on the LDHs/rGO Hybrid with significantly enhanced heck reactivity. ACS Applied Materials & Interfaces 2020; 12: 50365-50376. https://doi.org/10.1021/acsami.0c09106

51. Dong XQ, Lu SX, Xu WG, Li SG. The fabrication composite material of bimetallic micro/nanostructured palladium-platinum alloy and graphene on nickel foam for the enhancement of electrocatalytic activity. New Journal of Chemistry 2021; 45: 6550-6559. https://doi.org/10.1039/d1nj00196e

52. Ren GH, Zhang ZC, Liu YJ, Liang Y, Zhang XC et al. One-pot solvothermal preparation of ternary PdPtNi nanostructures with spiny surface and enhanced electrocatalytic performance during ethanol oxidation. Journal of Alloys and Compounds 2020; 830. https://doi.org/10.1016/j.jallcom.2020.154671

53. Xu CX, Wang L, Mu XL, Ding Y. Nanoporous PtRu Alloys for Electrocatalysis. Langmuir 2010; 26: 7437-7443. https://doi.org/10.1021/la9041474

54. Wen CN, Li ZP, Cao CY, Wang YQ, Guo PZ et al. Structural evolution of palladium nanoparticles and their electrocatalytic activity toward ethanol oxidation in alkaline solution. RSC Advances 2016; 6: 91991-91998. https://doi.org/10.1039/c6ra18146e

55. Chen SS, Yang ZZ, Wang AJ, Fang KM, Feng JJ. Facile synthesis of bimetallic gold-palladium nanocrystals as effective and durable advanced catalysts for improved electrocatalytic performances of ethylene glycol and glycerol oxidation. Journal of Colloid and Interface Science 2018; 509: 10-17. https://doi.org/10.1016/j.jcis.2017.08.063

Supporting information

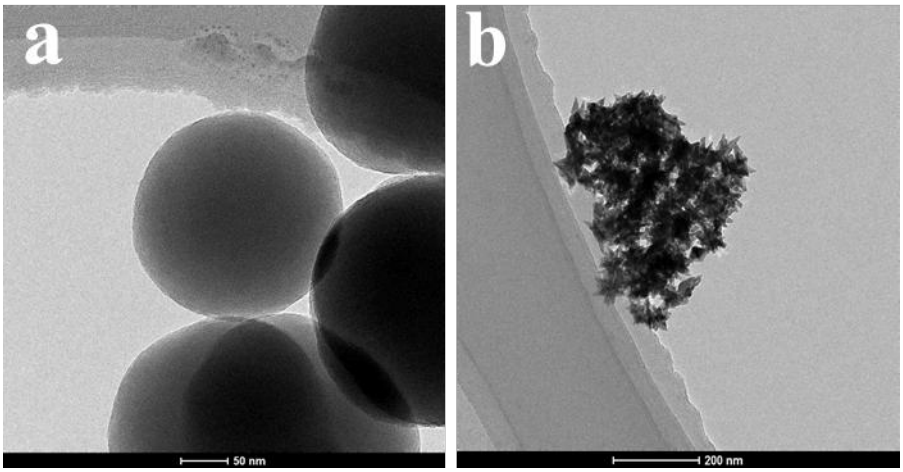

Figure S1. TEM images of SiO_2 nanospheres (a) and $Pd_4Cu_{(d)}$ alloys (b).

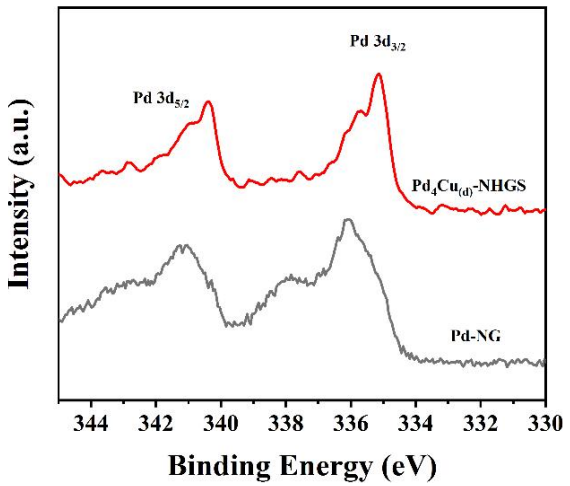

Figure S2. XPS spectra of $Pd_4Cu_{(d)}$-NHGS and Pd-NG.

Table S1. 2θ, d-spacing, lattice parameters, molar ratio, and Da of the catalysts.

Catalysts	**Plane**	**2θ/degree**	**d-spacing/Å**	**a /Å**	**Molar ratio (ICP)**	**Da /%**
Pd-NG	111	40.12	2.245	3.884		
	220	68.23	1.379			
$Pd_4Cu_{(d)}$-NHGS	111	40.46	2.235	3.845	2.60 : 1	54.17
	220	69.02	1.364			
$Pd_2Cu_{(d)}$-NHGS	111	40.60	2.228	3.835	2.26 : 1	59.75
	220	69.21	1.361			
$Pd_1Cu_{(d)}$-NHGS	111	40.75	2.220	3.820	2.04 : 1	71.91
	220	69.52	1.356			

Table S2. Comparison of current density and ECSA for EOR using different Pd-based electrocatalysts in alkaline medium.

Catalysts	Scan rate (mV/s)	ECSA (m^2/g)	Current density (mA/mg)	Reference	Year
$Pd_{68}Ni_{32}$/rGO	50	142	1820	[9]	2018
Pd_3NiP/N-rGO	50	83	2223	[11]	2020
PdAu NW	50	96	2253	[18]	2021
Pd@Cd_3-Ag_1	50	78	2928	[19]	2021
FePd-$Fe_2O_{3(3:5)}$/MWNTs	50	120	1191	[23]	2015
PdCu-3	50	25	1230	[24]	2020
$PdCu_{(F)}$-RGO	50	152	2416	[45]	2017
$Pd_4Cu_{(d)}$-NHGS	50	59	2683	This paper	--
10% Pd/C	50	24	1035	--	--